Supporting information

Probing Electrolyte Influence on CO_2 Reduction in Aprotic Solvents

Reginaldo J. Gomes†, Chris Birch†, Morgan M. Cencer‡, Chenyang Li‡, Seoung-Bum Son§, Ira D. Bloom§, Rajeev S. Assary‡, and Chibueze V. Amanchukwu†*

†Pritzker School of Molecular Engineering, The University of Chicago, Chicago, IL, 60637

‡Materials Science Division, Argonne National Laboratory, Lemont, IL, 60439

§Chemical Sciences and Engineering Division, Argonne National Laboratory, Lemont, IL, 60439

*Corresponding author

Email: chibueze@uchicago.edu

Cell setup and product distribution analysis

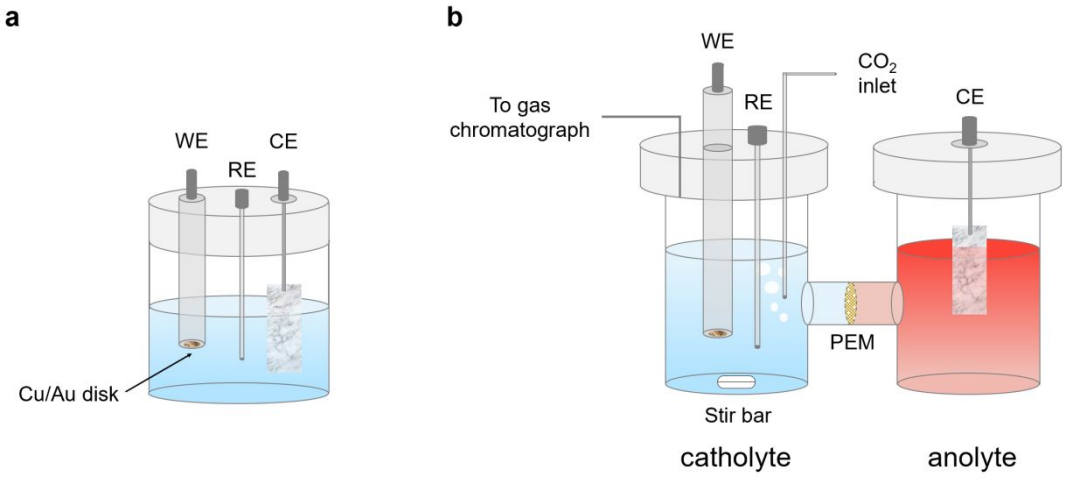

Figure S1. Illustration of (a) a beaker cell and (b) an H-cell cell setup, where WE is the working electrode (either Cu disk 31.6 mm^2 or Au disk 7.07 mm^2), RE represents the reference electrode (leakless Ag/AgCl), CE is the counter electrode (platinum foil), and PEM is the proton exchange membrane (Nafion® N-117). For the H-cell setup, stirring was kept at 1000 rpm with a CO_2 flow rate of 10 sccm.

The product distribution was investigated using an H-cell setup, coupled with a gas chromatograph (GC), as illustrated in the figure above. The faradaic efficiency values (FE) for the products in the gas phase were calculated as

$$FE\ (\%) = \frac{n_i * F * \phi_i * C_i}{I} \quad (1)$$

where n_i is the number of the electrons required for each CO_2 reduction product (e.g. n equals 2 for CO and hydrogen, or equals 8 for methane); F is the Faraday constant; ϕ_i is the molar flow rate for the carrier gas (either CO_2 or Argon); C_i is the concentration for each component read by the GC, and I is the average of the current obtained over 10 min before each injection on the GC.

Products in the liquid phase were analyzed by ^{1}H-NMR. Formic acid (FAc) was the only product observed in the liquid phase. So, different standard curves for FAc were constructed for each of the solvents here investigated, as indicated in Figure S2. The normalized area was calculated by the ratio between the area of the FAc and the area of

the internal standard, as previously described by Kuhl *et. al* [1]. We chose phenol (5mM in DMSO-d6) as an internal standard because it resonates close to FAc peak without overlaping with its signal. Moreover, phenol solutions in DMSO are stable over long periods. By using the normalized area, we can then minimize interferences in the ^{1}H-NMR signal caused by changes either in the solution compositions, NMR tube quality, or number of scans. To decrease the interference caused by solvent peak and enhance the formic acid signal, the center of the ^{1}H-NMR spectrum was set at 8.5 ppm, with a spectral width of 5 ppm, and number of scans of 40. FAc peaks were observed between 8 and 9 ppm depending on the sample composition.

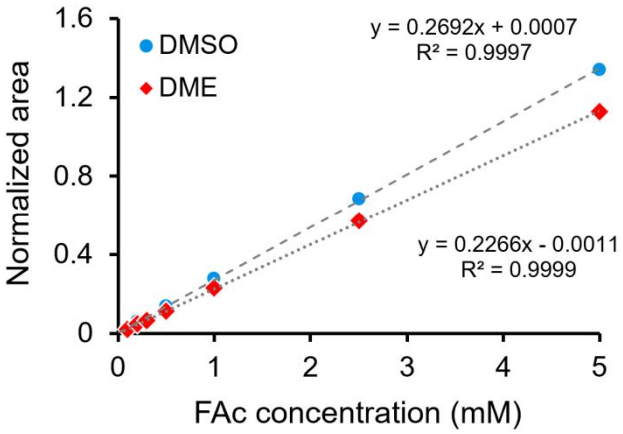

Figure S2. Standard curves constructed with FAc standards in DME and DMSO solutions containing 0.5M $TBAClO_4$ and 5mM phenol. DMSO-d6 was used as the deuterated solvent.

Liquid samples were extracted after 1.5h electrolysis for each one of the applied potentials. Since FAc accumulates in the catholyte chamber across potentials, the FE in the liquid phase was calculated taking into account the initial concentration of FAc before each of the applied potential as follows

$$FE\ (\%) = \frac{F * n_i * (C_j * V_j - C_{j-1} * V_{j-1})}{Q} \qquad (2)$$

where n_i is the number of the electrons required for each CO_2 reduction product (n equals 2 for FAc); F is the Faraday constant; C_j and V_j are the FAc concentration and catholyte volume for a sample from determining potential, while C_{j-1} and V_{j-1} represent the FAc

concentration and catholyte from the predecessor sample; and Q is the total charge collected for the specific applied potential.

Since H-Cell measurements were conducted inside of a glove box, any pressure fluctuations inside of the box may affect the CO_2 molar volume, adding uncertainties to the calculation of faradaic efficiency of the gaseous products (Equation 1 in the S.I.). Solvent evaporation also leads to a positive error for the FE calculations for the liquid products (Equation 2 in the S.I.). Since the sum of the FE values oscillate from 100 to 130% for some electrolytes, we opted to normalize all FE values to 100%, allowing a better comparison across the product distribution of different samples.

XPS studies

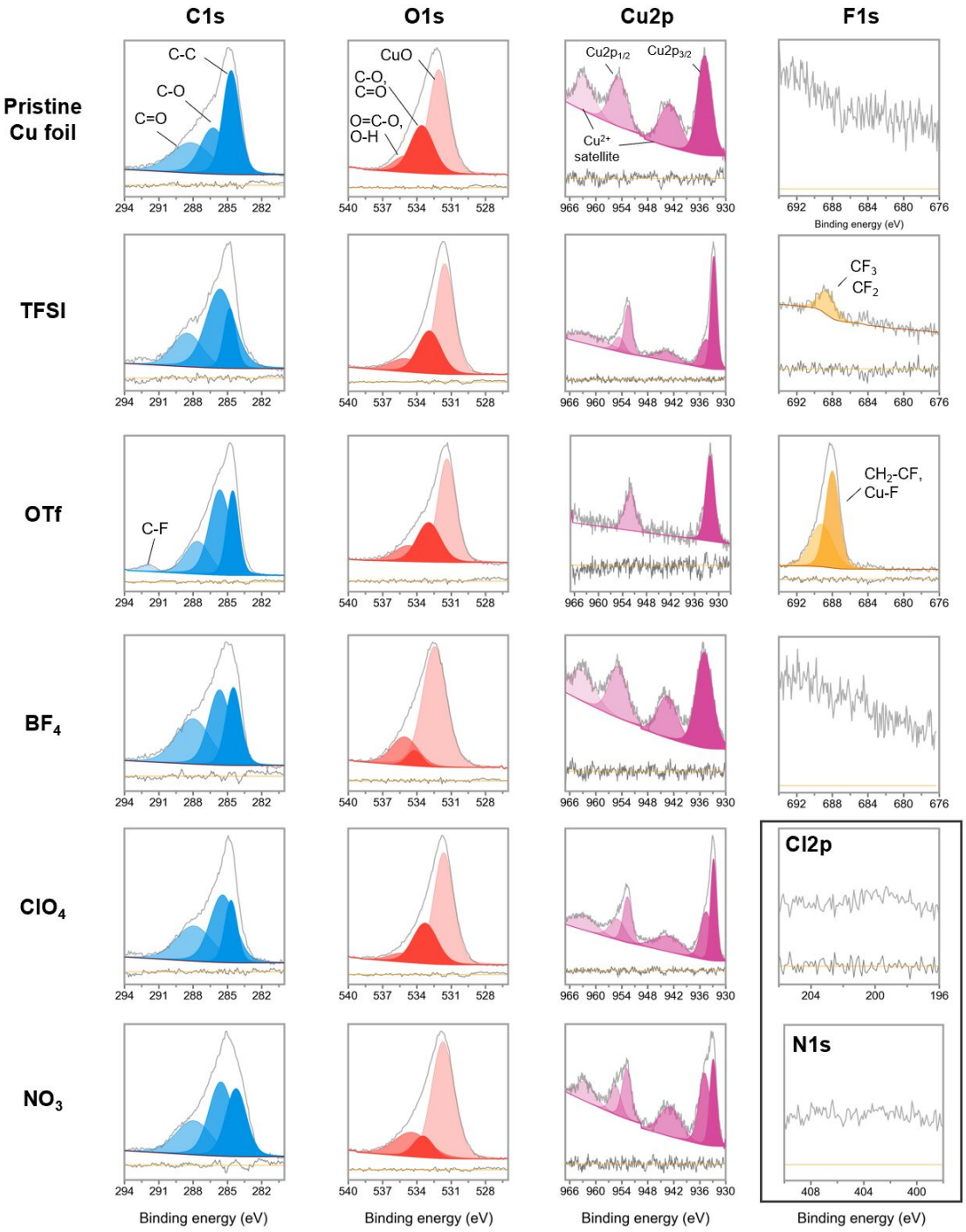

Figure S3. Probing catalyst and electrolyte stability. High-resolution XPS (X-ray photoelectron spectroscopy) of metallic copper electrodes before CO_2RR (Cu pristine foil) and after 10 min electrolysis at -2.0 V vs Fc* in DME in the presence of different TBA salts (0.5 M). All XPS samples were rinsed three times with DME before analysis

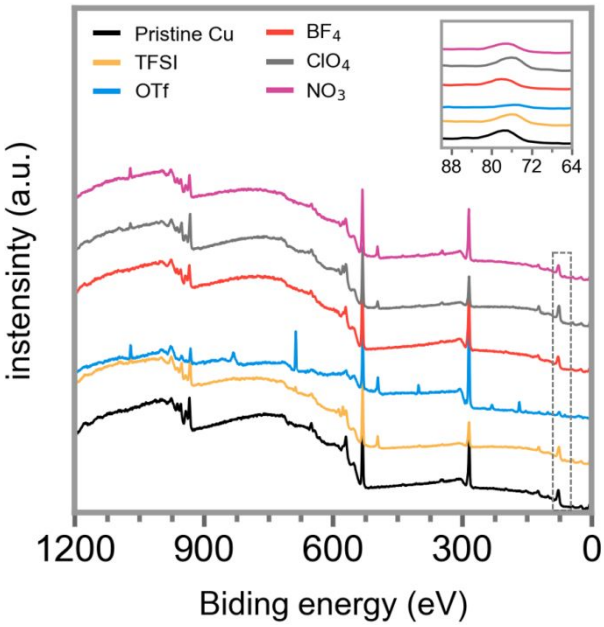

Figure S4. Investigating Pt deposition over the working electrode. Overall XPS survey spectra of metallic copper electrodes before CO_2RR (Cu pristine foil) and after 10 min electrolysis at -2.0 V vs Fc^* in DME in the presence of different TBA salts (0.5 M). All XPS samples were rinsed three times with DME before analysis. The highlighted area indicates the most likely location for the Pt, PtO, and PtO_2 peaks to be found [2,3].

Gravimetric determination of CO_2 solubility in glyme-ethers.

CO_2 solubility was done using a modification of the reported procedure[4]. Pristine glyme-ether solvents were first purged with Argon gas for 10 min to displace any dissolved CO_2 gas. Then, an aliquot of 1 mL of the glyme-ether sample was mixed with 7 mL of a 0.1M $Ba(OH)_2$ solution in water and used as a control. The remaining glyme-ether samples were purged with CO_2 (10 SCCM) for 10 min and 1ml of the sample aliquot was mixed with the $Ba(OH)_2$ solution as previously described. Later, both control and CO_2-containing samples were gently stirred for 10min. The precipitate was filtered with two stack layers of the Whatman™ quantitative filter papers (Grade 50 Circles) with the help of a Buchner funnel and a vacuum pump. Before the filtration, the quantitative filter papers were stored under vacuum until a constant weight was obtained. After filtration, the paper filters containing, the carbonate precipitates were heated at 120°C in a vacuum oven until constant weight. The CO_2 solubility was determined based on the amount of $BaCO_3$ formed, according to the following equation:

$$Ba(OH)_{2\,(aq)} + CO_{2\,(aq)} \rightarrow BaCO_{3\,(s)} + H_2O_{(l)} \quad (3)$$

$$CO_{2\,solubility}\,(mmol/l) = \frac{(m_2 - m_1) - (m_{2c} - m_{1c})}{MM_{BaCO_3} * V_{aliquot}} \quad (4)$$

Where m_1 and m_{1c} are the mass of the paper filter before filtration for the samples and control respectively; m_2 and m_{2c} are the mass of the paper filter after filtration for the samples and for the control, respectively; MM_{BaCO3} is the molar mass of $BaCO_3$; and $V_{aliquot}$ is the sample aliquot (1 mL).

Voltammetric studies

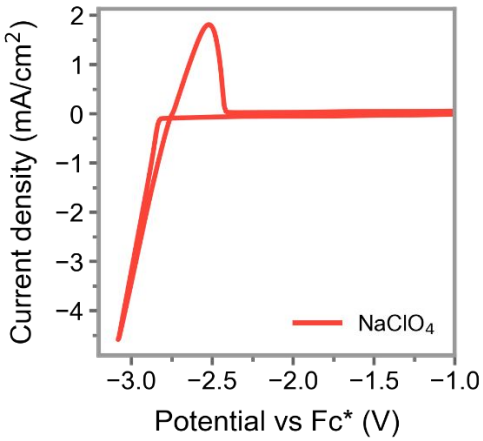

Figure S5. Sodium plating/stripping. Cyclic voltammogram for Cu electrode at 50 mV/s in Argon atmosphere in the presence of 0.5M $NaClO_4$ in DME.

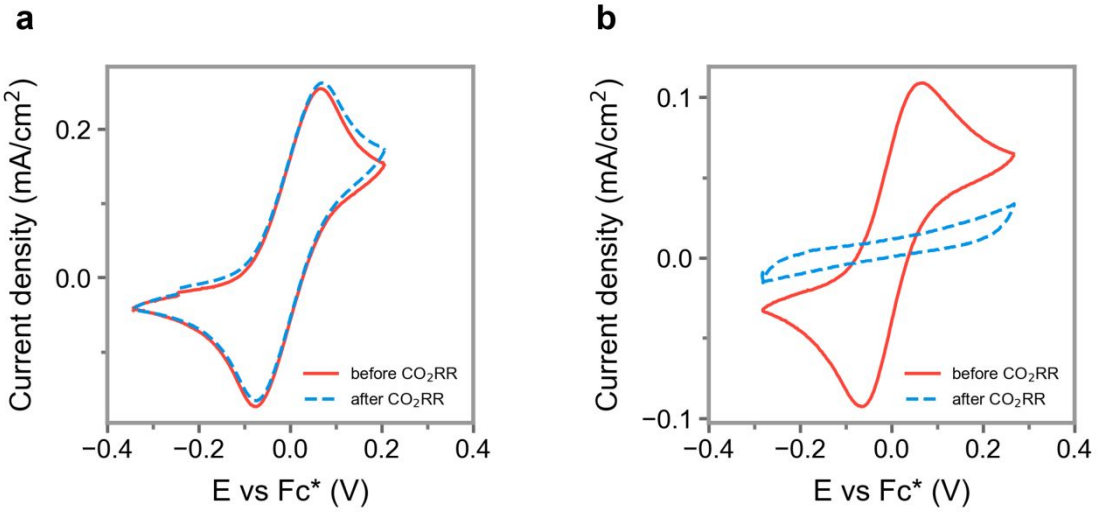

Figure S6. Effect of the alkali cation on electrode passivation. Cyclic voltammogram for Cu electrode at 50 mV/s in CO_2 atmosphere and 2mM decamethylferrocene (Fc*) in the presence of (a) 0.5 M $TBAClO_4$ and (b) 0.5 M $NaClO_4$ before (solid red lines) and after (dashed blue line) electrolysis. Both solutions were purged with CO_2 for 30 seconds to remove the excess of CO between the experiments.

Probing the solubility of carbonate species in DME

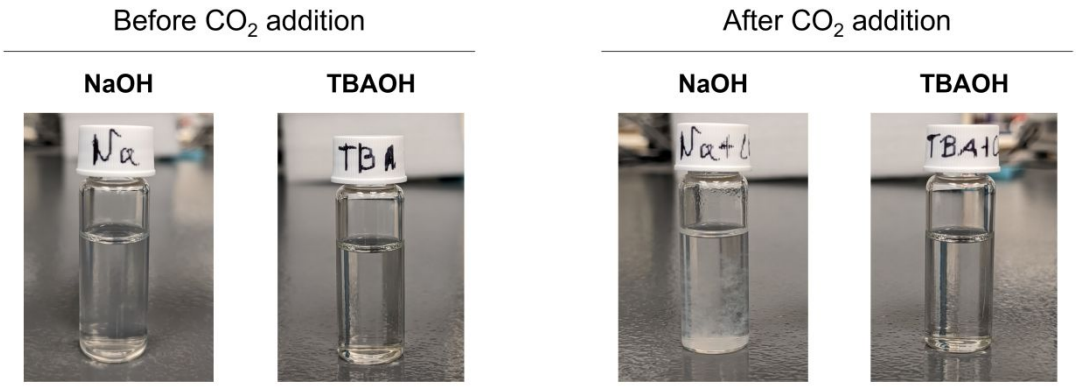

Figure S7. DME solvent samples containing 150mM of water and 5mM NaOH and 5mM TBAOH (left) and same solutions upon introduction of CO_2 at 20 sccm for 5min (right).

Determination of the water content

The water content of the different solvents and TBA solutions was measured by coulometric Karl-Fisher titration with a Mettler-Toledo C30S. Even though all electrolyte

solutions were prepared under dry conditions (below 100 ppm of water), the water content in the catholyte increased by one order of magnitude during CO_2RR (see Table S1). We hypothesize three sources for the water content increase: (i) Electrolytes can absorb moisture even from the inert Argon glovebox environment over the 12h experiment; (ii) Water can be generated *in situ*. The small amount of water could allow the CO_2RR to go through either a proton transfer or a proton-coupled electron transfer reaction[5]. Then, the generated OH^- could react with the protons that arise from the PEM, therefore forming more water; (iii) Water could also diffuse from the anolyte to the catholyte through the PEM[6]. Regardless of its source, water is most likely the main source of protons for the hydrogen gas observed in our product distribution analysis.

Table S1. Water content of the solvents

Solvent	Water content (ppm)
DME	6.0
DGME	6.5
TGME	14.5
DMSO	<1

Table S2. Water content for TBA supporting electrolytes in DME and DMSO after 30 min LSV experiments and after 12h GC experiments inside of an argon-filled glove box (water content < 1 ppm)

TBA solution (0.5 M)	**DME**		**DMSO**	
	After LSV (ppm)	After GC (ppm)	After LSV (ppm)	After GC (ppm)
TFSI	34.5	1035	41.9	-
OTf	55.7	1283	46.7	1302
BF_4	37.5	1258	80	-
ClO_4	51	2255	55.5	-
NO_3	40.5	1158	65.5	506

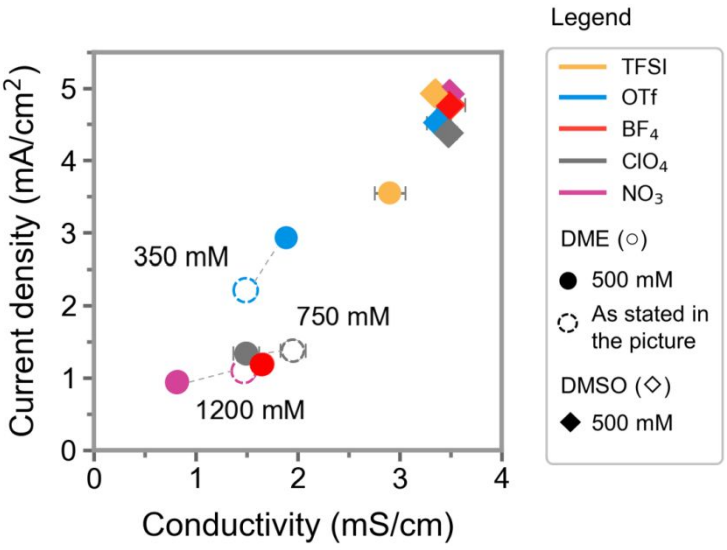

Figure S8. Conductivity of solutions containing different TBA salt concentrations in DME and DMSO *vs* current density extracted from the respective voltammograms at -2.8V vs Fc^* and scan rate of 50mV/s.

NMR studies

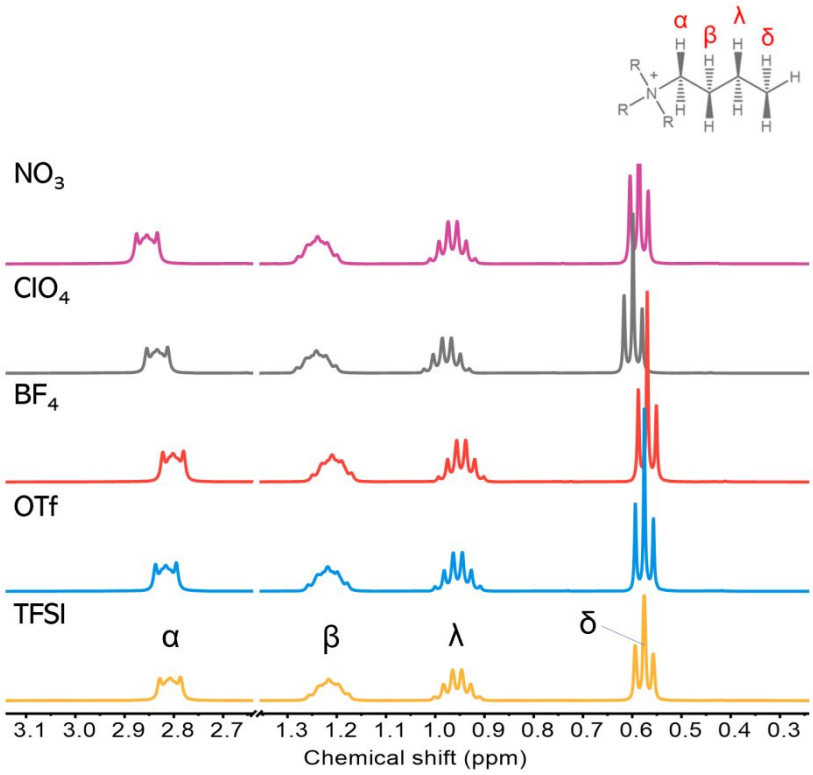

Figure S9. 1D ^{1}H-NMR for different TBA salts (0.5M) in DMSO.

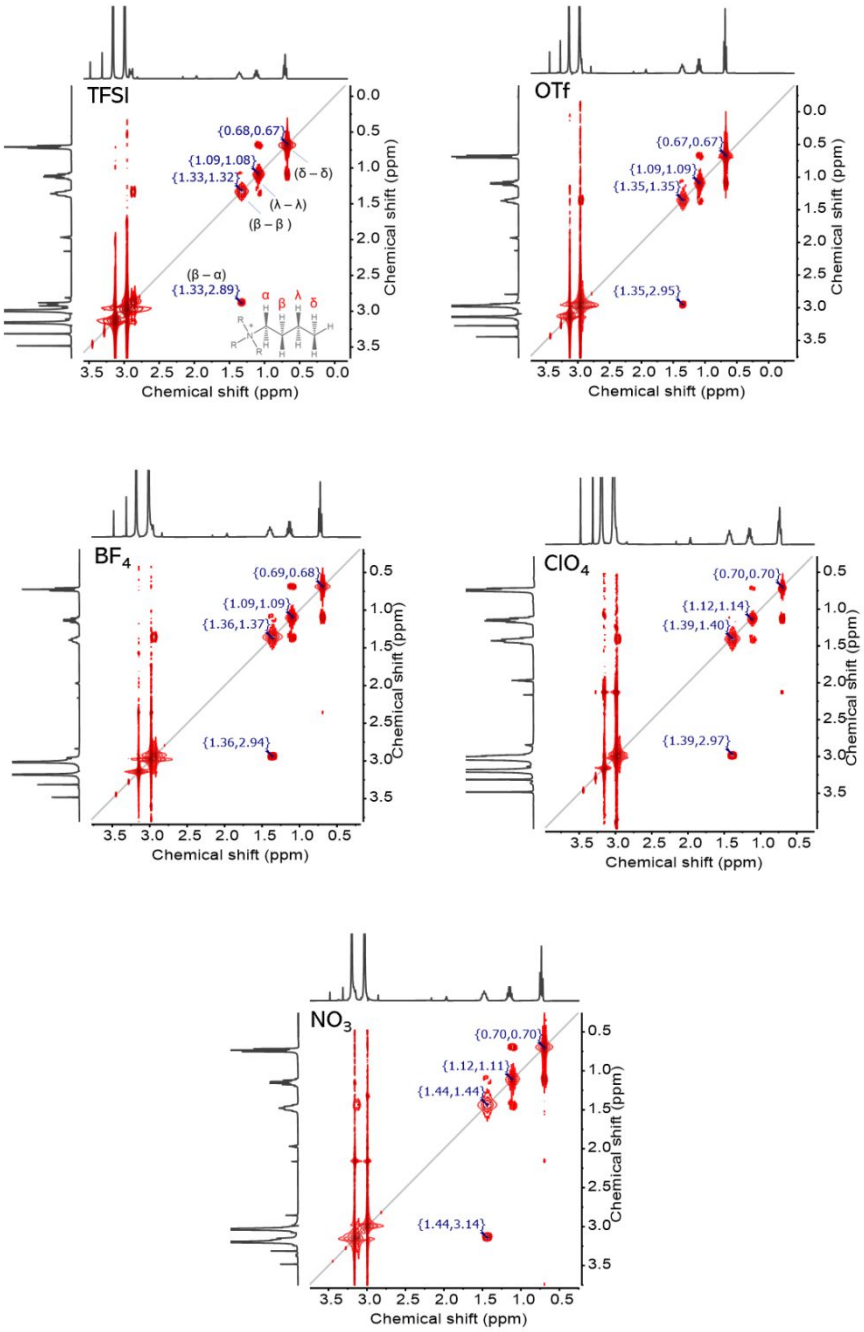

Figure S10. ^{1}H-^{1}H NMR COSY correlation spectrum for different TBA salts (0.5M) in DME. The chemical shift values for the α-H position were extracted from the β–α cross-peaks. The chemical shift values for the remaining hydrogens in the TBA were calculated as the average of the respective diagonal peaks.

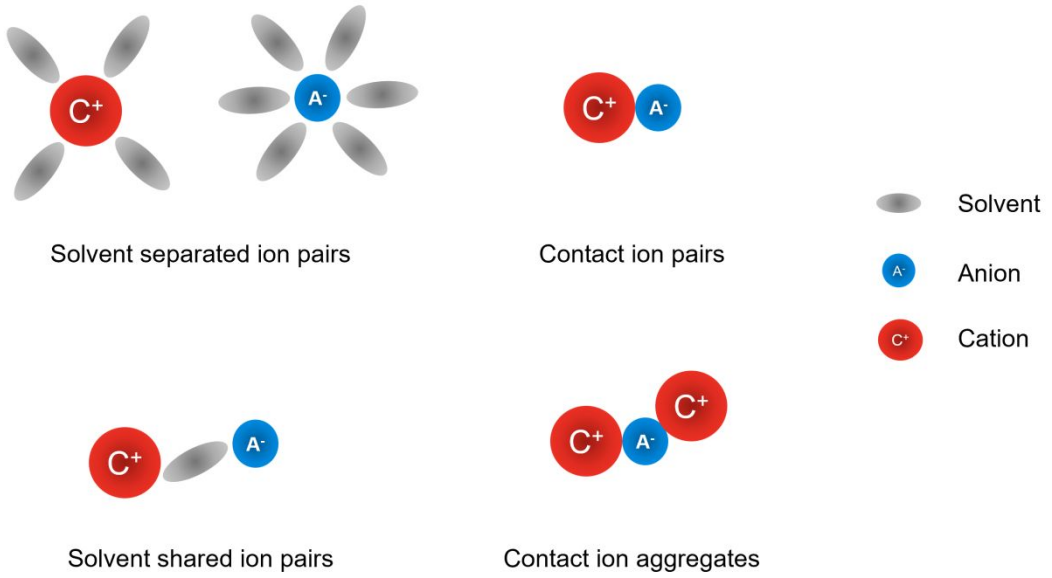

Figure S11. Ion solvation. Illustration of different ion solvation structures

Computational details

1. Density functional theory (DFT)

All DFT calculations of ion pairs formation were performed using Gaussian 16 at the ωb97XD/6-31+G(d,p) level of theory[7,8]. All geometries were optimized, and frequencies were evaluated at the same level of theory (Multiple conformers are considered). Numerical integrations were carried using ultrafine grids. To account for solvation in DME (ϵ = 7.2) and DMSO (ϵ = 46.8), self-consistent reaction-field (SCRF) using the conductor-like polarizable continuum model (CPCM) was employed in the calculation[9,10].

2. Complexation enthalpy (ΔH)

The complexation enthalpy (Δ*H*) of a complex ($TBA^+ + X^-$) was computed using:

$$\Delta H = H(TBA^+ + X^-) - H(TBA^+) - H(X^-), \quad (5)$$

where X^- represents anion species ($TFSI^-$, OTf^-, ClO_4^-, BF_4^-, and NO_3^-).

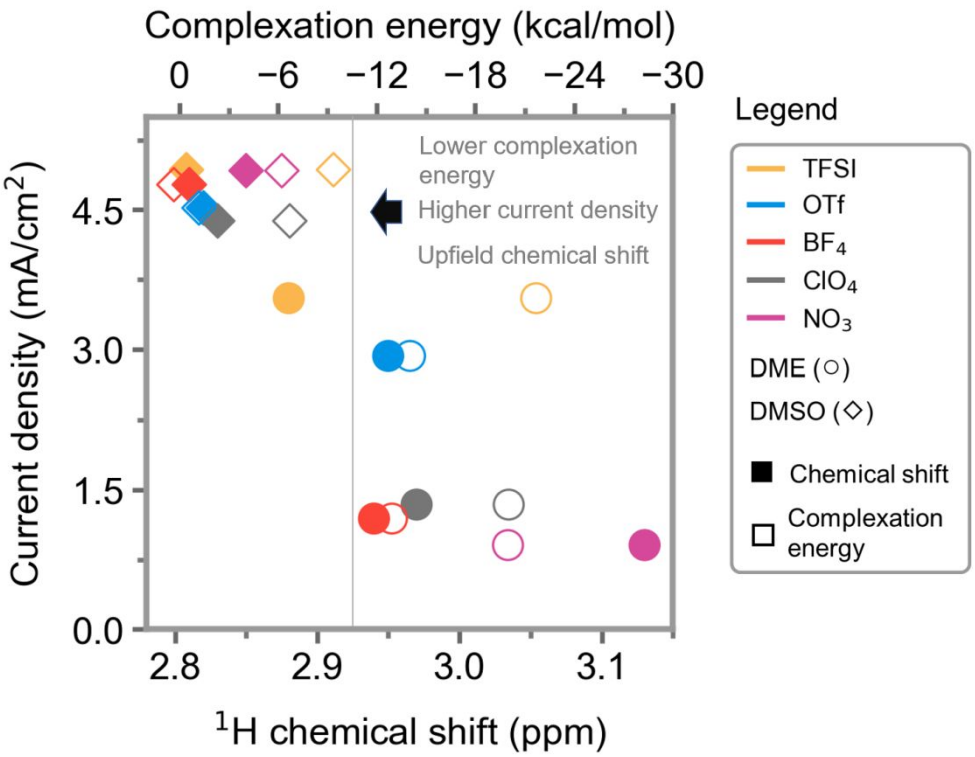

Figure S12. Correlation between the current density extracted from the LSVs plots (Figures 3a and 3c) at -2.8V vs Fc^* for Cu electrodes for different TBA salts in DME (circles) and DMSO (diamonds) *vs* (i) α-H chemical shifts from the TBA^+ (hollow icons) extracted from ^1H NMR results (Figures 4b and 4c) and (ii) complexation energy.

Measurements of the electrochemical double-layer capacitance (C_{dl})

Electrochemical double-layer capacitance values were measured in a single-chamber cell setup, with a leakless Ag/Ag^+ as a reference electrode, Au disk as a working electrode, and a platinum foil as a counter-electrode. To investigate the C_{dl} in the non-faradaic region, cyclic voltammograms were reordered at ± 0.15V against the open circuit potential (OCV) over different scan rates. The doble-layer charging is given by the average of the anodic (j_c) and cathodic (j_a) currents at OCV divided by the scan rate (v). Therefore, the C_{dl} values can be then extracted from the slope of the plot of current average and scan rate as follows,

$$C_{dl} = \frac{(J_a - j_c)}{v * 2} \quad (6)$$

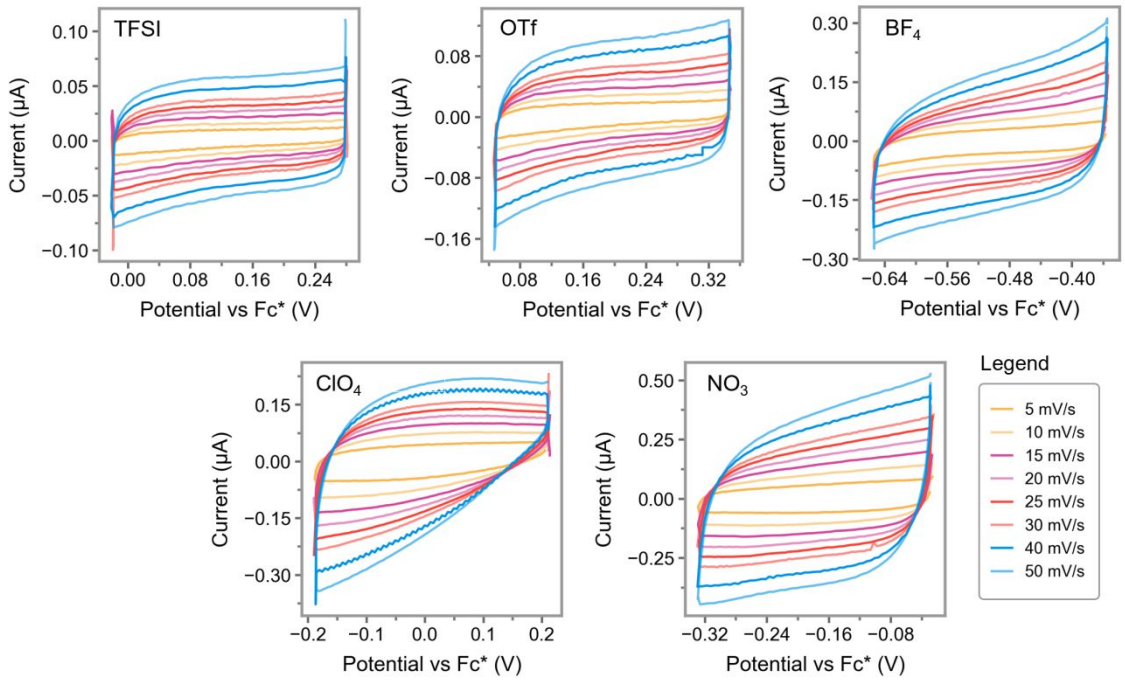

Figure S13. Cyclic voltammograms for Au electrode at different scan rates in Ar atmosphere in the presence of different electrolytes (0.5 M). The electrodes were rested in the respective electrolyte solutions for 5min for the stabilization of the OCV value before running the experiments.

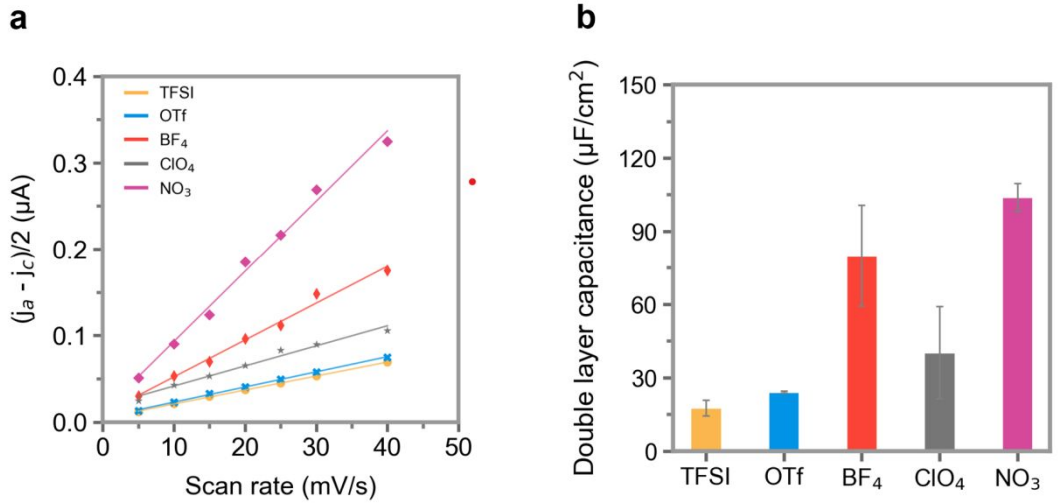

Figure S14. Average current at OCV *vs* scan rate extracted from the cyclic voltammograms in Figure S13 for different electrolytes in DME (a); C_{dl} values calculated from multiple electrolyte samples (b).

The C_{dl} values in the faradaic region was measured through electrochemical impedance spectroscopy (EIS) by fitting the experimental data to the simulation of the circuit depicted on Figure S15, where R_s is the solution resistance, R_{ct} is the charge transfer resistance, and CPE is the constant phase element. The C_{dl} values were calculated according to the Equation 7[11], where *n* is the exponential factor of the CPE. When *n* is equal to the unit, the interface presents pure capacitive behavior.

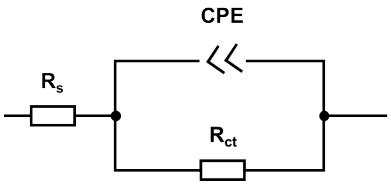

Figure S15. Equivalent circuit diagram for simulation of experimental EIS Nyquist plots. Rs is the series resistance, RCT is the charge transfer resistance, and CPE is the constant phase element

$$C_{dl} = [R_{CT}{}^{(1-n)} * CPE]^{\frac{1}{n}} \quad (7)$$

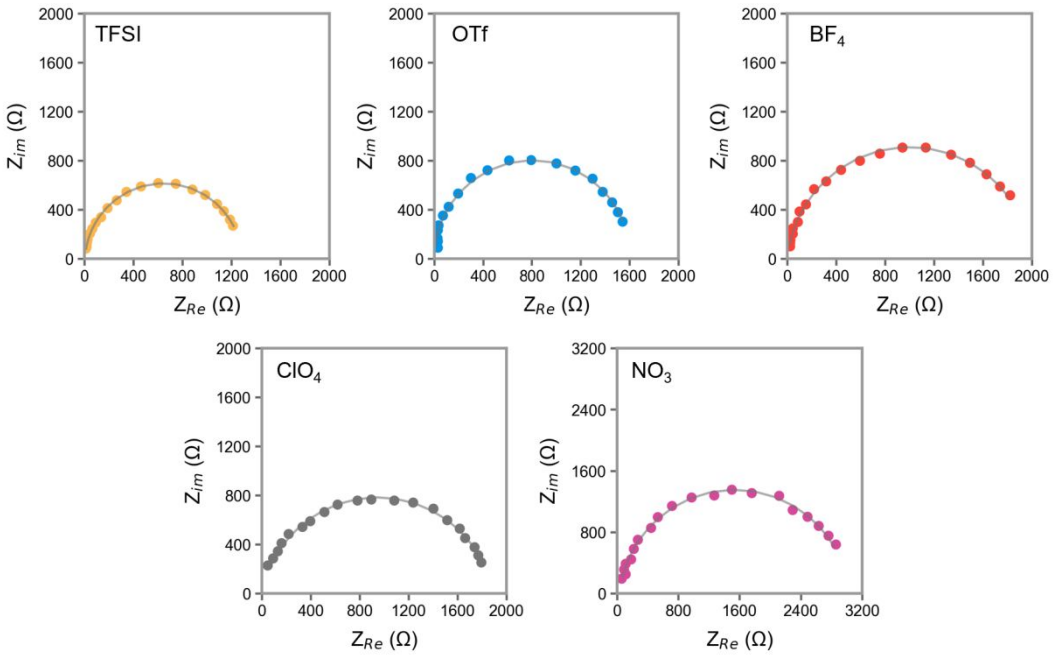

Figure S16. Nyquist plot (experimental and fitting for circuit simulations) for EIS experiments carried out in DME in the presence of different electrolytes (0.5M) under CO_2 atmosphere over a Au electrode (7.07 mm^2). Data were collected at -2.6V *vs* Ag/Ag^+ (-2.75 ± 0.03 V vs Fc*) from 100 kHz to 100 Hz, with a sinus amplitude of approximately

100 mV. The fitting for Nyquist plot simulation were made with the Python package impedance.py 1.40[12].

Table S3. Fitting parameters for the simulation of the Nyquist plots for multiple samples in DME.

	R_s (Ω)	R_{CT} (Ω)	CPE (μ F. s^{n-1})	n
TFSI	0.0 ± 0.0	1115 ± 186	0.33 ± 0.02	0.98 ± 0.02
OTf	3.6 ± 0.7	1572 ± 709	0.32 ± 0.01	0.99 ± 0.02
BF_4	7.3 ± 8.7	1680 ± 232	0.26 ± 0.06	0.97 ± 0.02
ClO_4	2.1 ± 3.0	1660 ± 50	0.22 ± 0.02	0.97 ± 0.03
NO_3	1.0 ± 1.0	3140 ± 20	0.23 ± 0.01	0.90 ± 0.01

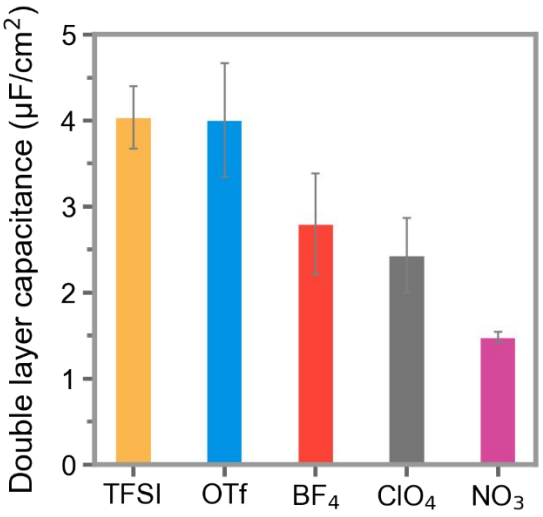

Figure S17. Double layer capacitance values at -2.6 V vs Ag/Ag^+ (-2.75 ± 0.03 V vs Fc*) for different electrolytes in DME (0.5M) for an Au electrode in CO_2 atmosphere.

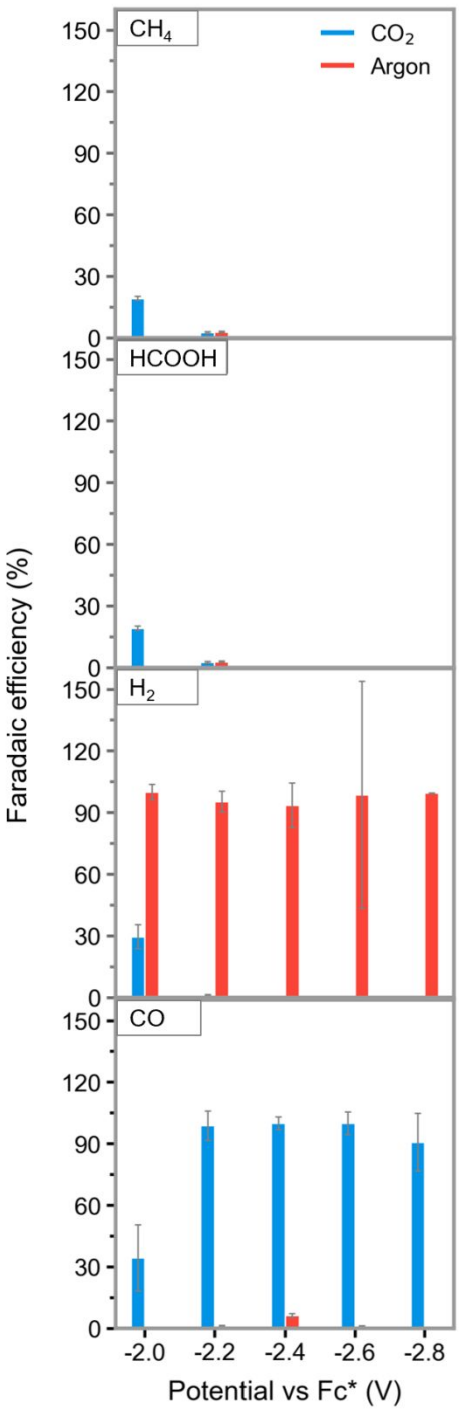

Figure S18. CO_2RR product distribution under CO_2 (blue bars) and Argon atmosphere (red bars) in 0.5 TBAOTf in DME as catholyte and $TBAClO_4$ (0.5M) containing 0.5M of water in DME as anolyte. Cu disk (31.67 mm^2) was used as a cathode, an Ag/AgCl leakless electrode was used as a reference electrode, and Pt foil was used as an anode.

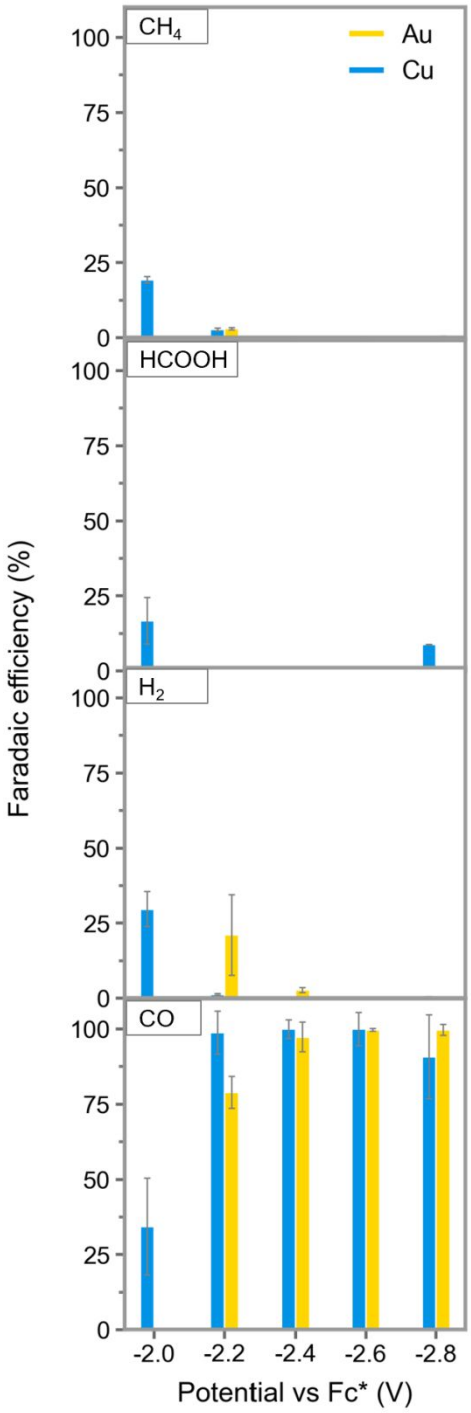

Figure S19. CO_2RR product distribution for different electrodes in 0.5 TBAOTf in DME as catholyte and $TBAClO_4$ (0.5M) containing 0.5M of water in DME as an anolyte. Cu disk (31.67 mm^2) and Au disk (7.07 mm^2) were used as a cathode, an Ag/AgCl leakless electrode was used as a reference electrode, and Pt foil was used as an anode.

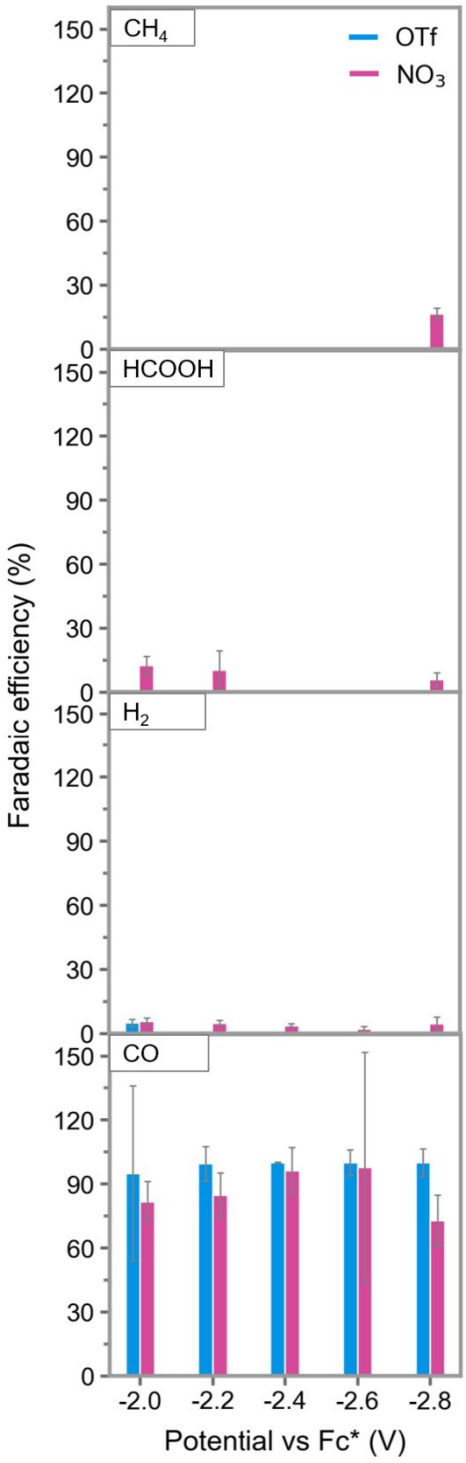

Figure S20. CO_2RR product distribution for different TBA salts in DMSO. 0.5M TBAOTf and 0.5M $TBANO_3$ were used as catholyte while $TBAClO_4$ (0.5M) containing 0.5M of water in DMSO as an anolyte. Cu disk (31.67 mm^2) was used as a cathode, Ag/AgCl leakless electrode was used as a reference electrode, and Pt foil was used as an anode**.**

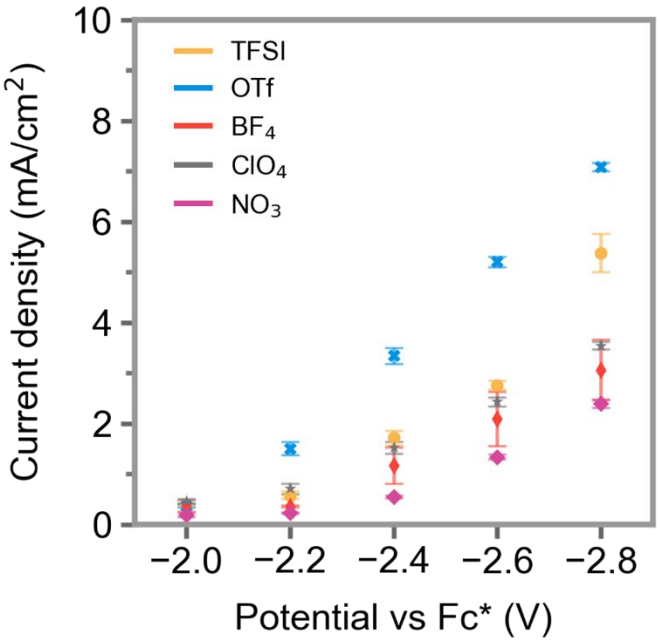

Figure S21. Current density values for different electrolytes in DME during H-cell measurements for multiple samples.

References

(1) Kuhl, K. P.; Cave, E. R.; Abram, D. N.; Jaramillo, T. F. New Insights into the Electrochemical Reduction of Carbon Dioxide on Metallic Copper Surfaces. *Energy & Environmental Science* **2012**, *5* (5), 7050–7059. https://doi.org/10.1039/C2EE21234J.

(2) Ali-Löytty, H.; Hannula, M.; Valden, M.; Eilert, A.; Ogasawara, H.; Nilsson, A. Chemical Dissolution of Pt(111) during Potential Cycling under Negative PH Conditions Studied by Operando X-Ray Photoelectron Spectroscopy. *Journal of Physical Chemistry C* **2019**, *123* (41), 25128–25134. https://doi.org/10.1021/acs.jpcc.9b05201.

(3) Chen, R.; Yang, C.; Cai, W.; Wang, H. Y.; Miao, J.; Zhang, L.; Chen, S.; Liu, B. Use of Platinum as the Counter Electrode to Study the Activity of Nonprecious Metal Catalysts for the Hydrogen Evolution Reaction. *ACS Energy Letters* **2017**, *2* (5), 1070–1075. https://doi.org/10.1021/acsenergylett.7b00219.

(4) Mizen, M. B.; Wrighton, M. S. Reductive Addition of CO 2 to 9,10-Phenanthrenequinone. *Journal of The Electrochemical Society* **1989**, *136* (4), 941–946. https://doi.org/10.1149/1.2096891.

(5) Dunwell, M.; Luc, W.; Yan, Y.; Jiao, F.; Xu, B. Understanding Surface-Mediated Electrochemical Reactions: CO2 Reduction and Beyond. *ACS Catalysis* **2018**, *8* (9), 8121–8129. https://doi.org/10.1021/acscatal.8b02181.

(6) Thieu, L. M.; Zhu, L.; Korovich, A. G.; Hickner, M. A.; Madsen, L. A. Multiscale Tortuous Diffusion in Anion and Cation Exchange Membranes. *Macromolecules* **2019**, *52* (1), 24–35. https://doi.org/10.1021/acs.macromol.8b02206.

(7) Frisch, M. J.; Trucks, G. W.; Schlegel, H. B.; Scuseria, G. E.; Robb, M. A.; Cheeseman, J. R.; Scalmani, G.; Barone, V.; Petersson, G. A.; Nakatsuji, H.; et al. Gaussian 16; Gaussian, Inc.: Wallingford, CT, 2016.

(8) Chai, J.-D.; Head-Gordon, M. Long-Range Corrected Hybrid Density Functionals with Damped Atom–Atom Dispersion Corrections. *Physical Chemistry Chemical Physics* **2008**, *10* (44), 6615–6620. https://doi.org/10.1039/B810189B.

(9) Barone, V.; Cossi, M. Quantum Calculation of Molecular Energies and Energy Gradients in Solution by a Conductor Solvent Model. *The Journal of Physical Chemistry A* **1998**, *102* (11), 1995–2001. https://doi.org/10.1021/jp9716997.

(10) Cossi, M.; Rega, N.; Scalmani, G.; Barone, V. Energies, Structures, and Electronic Properties of Molecules in Solution with the C-PCM Solvation Model. *Journal of Computational Chemistry* **2003**, *24* (6), 669–681. https://doi.org/https://doi.org/10.1002/jcc.10189.

(11) Brug, G. J.; van den Eeden, A. L. G.; Sluyters-Rehbach, M.; Sluyters, J. H. The Analysis of Electrode Impedances Complicated by the Presence of a Constant Phase Element. *Journal of Electroanalytical Chemistry and Interfacial Electrochemistry* **1984**, *176* (1–2), 275–295. https://doi.org/10.1016/S0022-0728(84)80324-1.

(12) Murbach, M. D.; Gerwe, B.; Dawson-Elli, N.; Tsui, L. Impedance.Py: A Python Package for Electrochemical Impedance Analysis. *Journal of Open Source Software* **2020**, *5* (52), 2349. https://doi.org/10.21105/JOSS.02349.